A Green Solution to Energy Storage: Brewers' Spent Grains Biocarbon-Silica Composites as High-Performance Lithium-Ion Batteries Anodes

Sofía Raviolo, M. Victoria Bracamonte, Cecilia A. Calderón, Fernando P. Cometto and Guillermina L. Luque**

Sofía Raviolo,
Instituto de Física Enrique Gaviola (IFEG), CONICET
Facultad de Matemáticas, Astronomía, Física y Computación, Universidad Nacional de Córdoba (UNC)
postcode 5000, Argentina
E-mail: sofiraviolo@unc.edu.ar

María Victoria Bracamonte, Cecilia Andrea Calderón
Instituto de Física Enrique Gaviola (IFEG), CONICET
Facultad de Matemáticas, Astronomía, Física y Computación, Universidad Nacional de Córdoba (UNC)
Departamento de Química Teórica y Computacional, Facultad de Ciencias Químicas, Universidad Nacional de Córdoba (UNC)
postcode 5000, Argentina

Fernando Pablo Cometto
Instituto de Investigaciones en Físico-Química de Córdoba (INFIQC), CONICET
Departamento de Fisicoquímica, Facultad de Ciencias Químicas, Universidad Nacional de Córdoba (UNC)
postcode 5000, Argentina

Guillermina Leticia Luque
Instituto de Investigaciones en Físico-Química de Córdoba (INFIQC), CONICET
Departamento de Química Teórica y Computacional, Facultad de Ciencias Químicas, Universidad Nacional de Córdoba (UNC)

This article has been accepted for publication and undergone full peer review but has not been through the copyediting, typesetting, pagination and proofreading process, which may lead to differences between this version and the Version of Record. Please cite this article as doi: 10.1002/ente.202300342

postcode 5000, Argentina
E-mail: guillerminaluque@unc.edu.ar

Keywords: biocarbon, silica, lithium-ion battery, anode, brewing spent grains.

Abstract

The demand for more efficient energy storage devices has become increasingly important in order to face the ongoing energy transition. In this regard, it is equally important to attain the production of these devices with the lowest possible environmental impact. In light of this, the use of waste materials and low-polluting methods has become a strategic priority. In this study, brewers' spent grains were utilized as raw material to produce anodic electrodes for lithium-ion batteries. The synthesis process involves only two pyrolysis steps at low temperatures without any chemical treatment, reducing energy investment and waste generation. The result is a porous biocarbon structure - with mixed graphitic and amorphous characteristics - decorated with silica nanoparticles. The presence of silica greatly enhances storage capacity. The obtained biocarbon based electrodes exhibited a capacity of 455 mAh g^{-1} after 100 cycles, surpassing the standard anode material commonly used in commercial lithium-ion batteries.

1. Introduction

Modern society requires low-cost and environmentally sustainable energy storage and conversion devices, with lithium-ion batteries (LIBs) currently dominating the world market as the leading technology capable of reducing CO_2 emissions from transport [1]. LIBs offer several advantages over other storage systems, including higher voltage, increased safety, higher efficiency, and lighter weight [2]. However, the commonly used anode material in commercial LIBs, graphite, has limited lithium storage capacity (372 mAh g^{-1}), poor rate performance, and is difficult to recycle, making it insufficient for high energy demands in next-generation hybrid and electric vehicles [3,4].

Among new anode materials, soft and hard carbons have appeared as promising replacements for graphite. Soft carbons (SC) have been widely used in LIBs because of their large specific surface areas, high conductivities and storage capacities [5–7]. However, they are synthesized by high-cost processes, needing high purity raw materials which reduce their commercial applications. In contrast, hard carbons (HC) require simpler synthetic processes and cheap

environmentally friendly raw materials to produce. This fact and their controllable morphology and porosity, makes HCs great candidates for LIB anodes. The biomasses derived from renewable carbon-rich agro-industrial waste, including peanut shells, rice husks, walnut shells, and others [3,8–13], have gained special attention as source for HC due their tunable surface properties, low cost and potential to contribute to a more circular economy.

In this study, we propose an easy-to-scale-up, one/two-step pyrolysis method to develop macroporous and functionalized structures from brewer's spent grains (BSGs) as anode material for LIBs. BSGs are a common biowaste generated in breweries and represent about 85% of the total waste weight during brewing, with approximately 6.8 billion tons produced in Europe in tons in Europe in 2019[14]. BSG is primarily composed of cellulose, hemicellulose, and lignin, which contains hydrocarbon chains that form cross-linked and hierarchical frameworks. Moreover, barley plant tissue is also composed of small amounts of silica (SiO_2) [12,14–16], making them an ideal candidate for producing C/SiO_x composites with higher specific capacities than graphite.

The BSGs obtained biocarbons were characterized by various physicochemical techniques and tested as LIB anodes, optimizing the electrode slurry using an aqueous-based binder. The electrochemical results demonstrated good reversibility and capacity retention, highlighting the potential to add value to a waste material from the brewery industry by using it as anodes for LIBs. This study underscores the importance of slurry preparation and the potential of using waste materials to contribute to the development of more efficient and sustainable energy storage devices.

2. Materials and Methods

2.1. Biochar synthesis

The brewery residues were initially washed with distilled water multiple times and subsequently dried in a vacuum oven at 80 °C overnight. The resulting material was then milled to obtain smaller grains and pyrolyzed in a tubular furnace (GSL-1700X-S-60UL) under an argon atmosphere at 400 °C for 3 hours with a heating rate of 5 °C min^{-1}. The obtained biocarbon was named BBC_400 and was used as the starting point for synthesizing the second biochar. For this case, the BBC_400 was further pyrolyzed for two hours at 700 °C with a heating rate of 3 °C min^{-1} under an argon atmosphere, and the resulting biochar was labeled as BBC_400-700. **Figure 1** displays a photograph of the raw BSG material and the two biocarbons that were obtained.

Figure 1. Raw BSG and obtained biocarbons: BBC_400 and BBC_400-700.

2.2. Materials characterization

Thermal gravimetric analysis (TGA) of raw BSG, BBC_400, and BBC_400-700 was carried out on a TGA Q600 (TA Instruments) under an N_2 atmosphere, by equilibrating at 100 °C and following a heating ramp rate of 10 °C min^{-1} up to 800 °C to investigate the decomposition course of the samples. Crystal structure was investigated by XRD patterns with a Panalytical X'Pert Pro diffractometer using Cu Kα radiation with wavelength λ=1.541 Å, a scanning range of 10º - 80º, scanning speed of 6 min^{-1}, voltage of 40 kV and current of 30 mA. The biocarbon's morphology was characterized by field-emission scanning electron microscopy (FE-SEM Zeiss) at 3 keV, while the chemical composition was determined by EDS attached to FE-SEM at 20 keV. Pore diameter and particle size determination were performed using the Image J software. To conduct the analysis, three micrographs were processed, each representing different parts of the sample, and they were deeply analyzed (pores and/or particles). The pores and particles were measured and the average diameter per zone was obtained. Subsequently, the final average diameter was calculated with these obtained values. Standard deviation was assigned as an error in the final calculation. Raman spectra were carried out by a Horiba Jobin-Yvon LabRam HR spectrometer using λ=633 nm with a range of 400-3400 cm^{-1}. X-Ray photoelectron spectrometry (XPS) measurements were performed with K-Alpha™ X-ray Photoelectron Spectrometer (using non-monochromatized Al-Kα 1200W). The fitting of the spectra was performed using the Avantage® and Igor software with a Shirley-type background. The BBC elemental composition was analyzed by atomic absorption spectrometer (AAS), Perkin Elmer AAnalyts 100.

2.3. Electrochemical test

Galvanostatic charge/discharge measurements were conducted using coin cells (CR 2032) assembled in an argon-filled glovebox (MBraun, O_2 and H_2O < 1 ppm) with lithium metal as counter and reference electrode, glass microfiber separator (Whatman GF/F), and 1 M lithium hexafluorophosphate ($LiPF_6$) dissolved in a 1:1 (V:V) mixture of ethylene carbonate (EC) and dimethyl carbonate (DMC) as the electrolyte. The anodes were prepared by mixing 80 wt.% BBC as the active material, 10 wt.% carboxymethyl cellulose (CMC) as a binder, and 10 wt.% Super P carbon. The electrode slurries were prepared using two different solvents: deionized water (BBC_400_water and BBC_400-700_water) and 0.1 M phosphoric acid (H_3PO_4) pH = 2, adjusted using potassium hydroxide (BBC_400_acid and BBC_400-700_acid). The slurries were coated onto a copper foil by doctor blade method and dried at 80 °C for 2 hours. Galvanostatic charge/discharge measurements were conducted to evaluate the cycling performance of the anodes. The measurements were carried out using a Biologic (Model BCS-810) galvanostat/potentiostat at varying C-rates, with the value of C fixed at the theoretical graphite capacity (372 mAh g^{-1}). The potential range for the measurements was set at 1.500 - 0.001 V.

3. Results and discussion

3.1. Physicochemical characterization

The above paragraph provides a detailed description of the physicochemical characterization of biochars synthesized from raw BSG by one/two steps pyrolysis methods. The yields obtained for BBC_400 and BBC_400-700 were 40 wt.% and 32 wt.%, respectively. **Figure 2** displays the thermogravimetric analysis for BSG and BBCs (and their differential thermal analysis is shown in **Figure S1**). The samples underwent an initial stabilization step at 100 °C to eliminate volatile compounds, primarily water, from the surface of the samples. The TGA curve of BSG reveals three primary stages, which are also discernible as three peaks in Figure S1. The first stage is associated with the decomposition of hemicellulose and takes place primarily between 220 ºC and 315 °C, with the maximum mass loss rate occurring at 280 °C. This decomposition process continues slowly at higher temperatures. The second stage is related to the degradation of cellulose, which occurs between 315 ºC and 400 °C, with the maximum weight loss rate attained at 350 °C. When the temperature is above 400 °C, almost all the cellulose is already pyrolyzed, and this leads to the third inflection point. This third

stage corresponds to the decomposition of hemicellulose and lignin. According to the literature [17], the degradation of lignin occurs over the entire temperature range, albeit at an extremely slow rate of mass loss. Based on the above, two pyrolysis procedures were selected for comparison, one at 400 °C and the other at 400 and 700 °C. By analyzing the TGA curves shown in Figure 2, it can be observed that the BBC_400 sample experiences a reduction in mass at temperatures exceeding 400 °C due to the degradation of cellulose and hemicellulose, as mentioned earlier. In contrast, the BBC_400-700 sample does not exhibit any mass loss in this temperature range, indicating the stability of its carbonization.

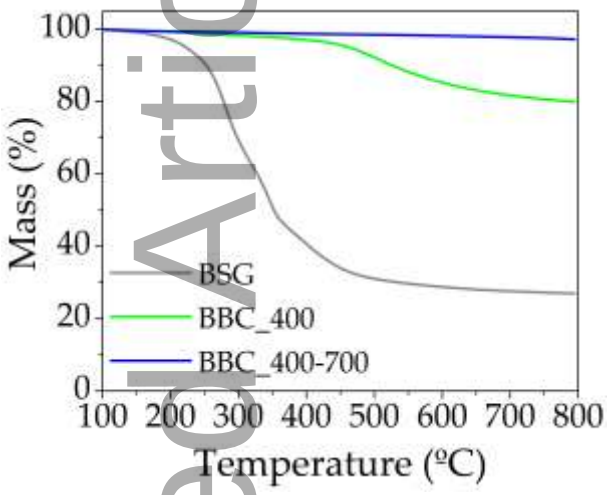

Figure 2. Thermogravimetric curves for BSG, BBC_400, and BBC_400-700.

Figure 3a and **b** show the X-ray diffractogram and the Raman spectroscopy spectrum for both carbon materials. The obtained diffractograms show two typical broad peaks around 24° and 43° associated with the diffraction of the (002) and (100) graphite planes, respectively for both biocarbons. The peak corresponding to (100) plane reflection indicates the presence of a honeycomb structure due to presence of sp2 hybridized carbon[18]. The broadness of the signals indicates the presence of disordered carbon in both materials[19]. BBC_400 sample shows 2 peaks at 23.5° and 42.5°, whereas for BBC_400-700 peaks appear at 23.9° and 43.7°. It can be seen that for the two-steps pyrolysis biochar, diffracted peaks have higher intensity. This result indicates that more graphitic phase is present in the BBC_400-700 sample. This observation is compatible with the fact that at higher pyrolysis temperature more hydrogen and oxygen atoms are eliminated from the material, increasing aromatic rings on graphitic layers and improving the crystallinity of the overall biocarbon[20,21]. To corroborate this conclusion, the inter-planar distances d002 were determined using Bragg's law resulting in 0.377 nm and 0.372 nm for BBC_400 and BBC_400-700, respectively. Even though both

values are higher than pure graphite (0.334 nm) due to the presence of a disordered carbon phase in both samples, the lower value obtained for BBC_400-700 indicates that this sample presents more graphitic phase, in agreement with previous observations.

This result is also confirmed by the Raman spectrum (Figure 3b) in which two peaks are observed at 1318 cm-1 and 1600 cm-1 attributed to the D (defect band, corresponding to the A1 g mode) and G (graphite band, corresponding to the E2g hexagonal graphitic lattice) band, respectively. On both samples the 2D band appears at 2700 cm-1, which corresponds to in-plane vibrations of sp2 hybridized carbon[22].

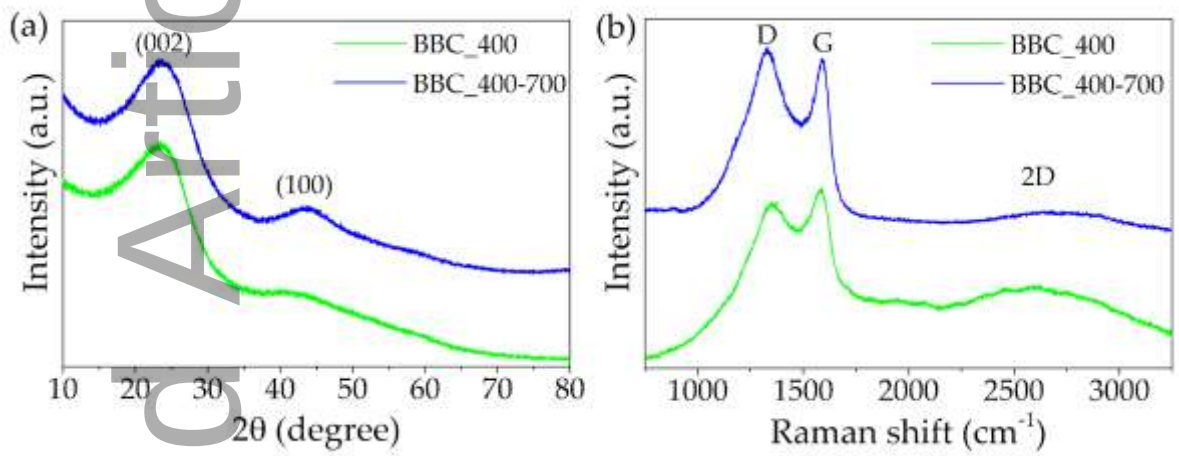

Figure 3. BBCs analysis: (a) XRD and (b) Raman spectra.

It is well known that the peak width as well as the I_D/I_G ratio (Raman intensity ratio) is a measure of perfect, imperfect and disordered structure of carbon materials [22,23]. For BBC_400 and BBC_400-700 samples I_D/I_G ratio is (0.94 ± 0.02) and (1.05 ± 0.02), respectively. This means that both, graphite and disordered structure are present, along with a high amount of defects/disorder in the carbon lattice in the two samples. But, as BBC_400-700 sample presents higher I_D/I_G ratio (compared to the BBC_400 sample), a greater degree of graphitic phase could be present in this sample, as it was observed by XRD. This effect could be explained due to the fact that at higher pyrolysis temperature, more hemicellulose and lignin from the raw material are decomposed, as was shown in the TGA analysis. This decomposition generates more pores, higher pore diameter and more defects on the obtained material, which increases the D peak's intensity[24–27].

The morphology of the materials was studied by SEM (**Figure 4**). Both BBCs present a shield-like structure (Figure 4a and b) formed by a honeycomb arrangement of closely packed macropores with an average diameter d_p = (4 ± 2) µm for BBC_400 and (5 ± 2) µm for BBC_400-700 (Figure 4 c and d respectively). The observed values are in line with the earlier

discussion, as higher pyrolysis temperatures typically result in greater material decomposition and, as a consequence, larger pores are obtained. This finding is consistent with the more disordered structure observed through Raman studies. Spherical particles located on top of the surface and inside the first row of pores (Figure 4 c, d, e and f) appear on both materials. On BBC_400 these particles appear to be covered by a film (Figure 4e and **Figure S2** with higher magnification), while on BBC_400-700 this film is not present (Figure 4 f). The spherical particles on the BBC-400-700 sample have an average diameter of $d_s = (8 \pm 3)$ µm. In the case of the BBC_400 sample, this value could not be correctly determined due to the presence of an organic film that covers the particles. It is important to note that BBC_400 samples needed to be covered by a thin layer of gold to ensure enough conductivity, in order to avoid electronic charging of the material under the electron beam for SEM measurements. Nevertheless, in the case of the BBC_400-700 sample, this pretreatment was not necessary due to the higher conductivity of this material proving its higher graphitization degree and thus higher conductivity.

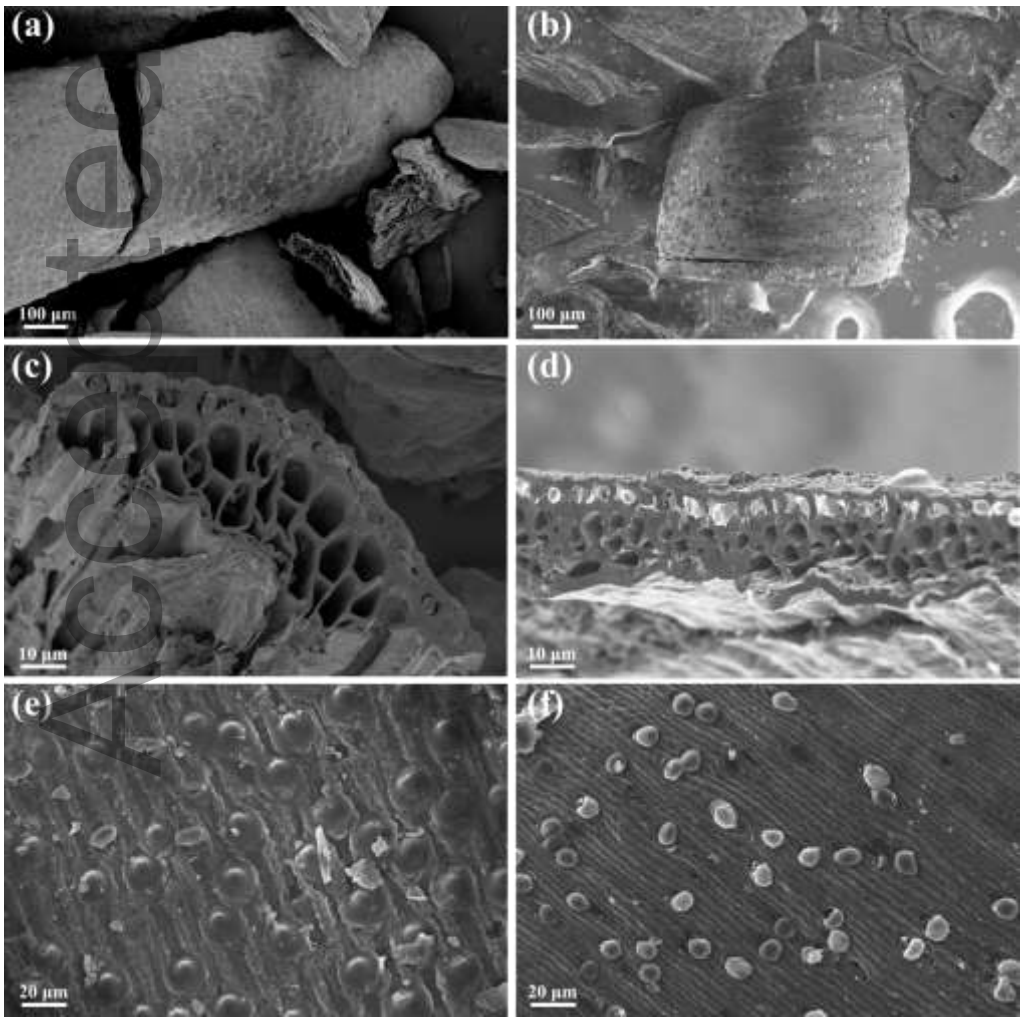

Figure 4. SEM images at different magnification levels: (a), (c) and (e) BBC_400, (b), (d) and (e) BBC_400-700.

An EDS analysis was performed to investigate the chemical composition of both the carbonaceous and particle materials. **Figure 5** shows the overlapping elemental maps of both samples (individual maps are shown in **Figure S3**) in which the SiO_x nature of the particles can be seen. Both samples are primarily composed of carbon and oxygen, with the BBC_400 sample exhibiting a higher and more dispersed oxygen content than BBC_400-700 (Figure S3 d and h). Additionally, the SiO_x particles in the BBC_400-700 sample are clearly defined and exposed on the surface, while the edges of the spheres in BBC_400 are less distinct and appear to be covered by a thin layer of carbon and oxygen that extends over the surface (Figure S2 and S3). The absence of this film in the BBC_400-700 sample indicates its decomposition with temperature and suggests that it may be composed of organic matter. The Si content of BBC samples is mainly attributed to phytoliths which originate from the silicon adsorbed from the soil by the plants[28].

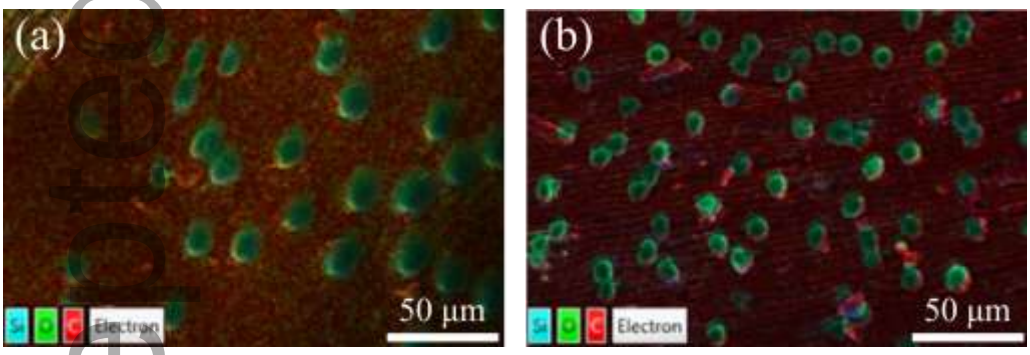

Figure 5. Overlapped SEM micrography and EDS elemental map: (a) BBC_400 and (b) BBC_400-700.

The elemental composition and the chemical environment present in the BBCs materials were analyzed by XPS. The survey spectra of both samples showed mainly the presence of C, O, Si and N with trace amount of P (**Figure S4**). Nevertheless, it is important to note that the ratio between C and O atoms calculated from XPS spectra increases after the second thermal treatment from 5.2 to 7.5, confirming the relative decrease of oxygenated carbon species due to thermal decomposition at higher temperatures. **Figure 6** a and b show XPS spectra of the C 1s region of BBC_400 and BBC_400-700 samples, respectively. These spectra show six deconvoluted peaks attributed to the different C species present in the samples. It can be observed that the main feature of BBC_400-700 sample is an asymmetric peak at 284.4 eV

attributed to carbon atoms with sp^2 hybrid orbitals, indicating that BBC_400-700 samples contain some degree of graphitization after thermal treatment (around 40 at.% of the total amount of C atoms). This peak is also present in the BBC_400 sample, but only represents the 10 at.% of the C species. These results are in agreement with the previous discussion about XRD and Raman results. The rest of the deconvoluted peaks in both samples located at 284.8 eV, 285.5 eV, 286.3 eV, 287.7 eV and 289.4 eV represent the C atoms in different environments, such as aliphatic C sp^3, C-OH, O-C-O, C=O and COOH, respectively [8,29–32]. Due to the low temperature treatment in BBC_400 sample, it is not surprising that the main C species are those described as non-graphitized species, such as C-C and C-H species (Figure 6 a). As stated above, the decrease on the relative amount of O atoms after thermal treatment can also be noted in the decrease in the relative areas of the features attributed to oxygenated species (from 36 % in the BBC_400 sample to 24 % in the BBC_400-700 sample).

Furthermore, Figure 6 c and d show XPS spectra of Si 2p region of BBC_400 and BBC_400-700 samples, respectively. At first sight, it can be observed that the Si 2p spectrum of BBC_400 sample is wider than the BBC_400-700 one. This fact, could be attributed to the attenuation of the photoelectrons derived from Si atoms due to the organic film that covers the Si particles in BBC_400 samples. This film has been removed after second thermal treatment, as it is evidenced in the shape of BBC_400-700 Si 2p spectra. Despite the widening of Si 2p spectrum due to this attenuation effect, after fitting, only one Si 2p doublet can be obtained in both samples. Here the Si 2p 3/2 feature is located at 103.3 eV which is attributed to the presence of SiO_2 species[33,34] confirming the presense of SiO_x particles as observed by EDS.

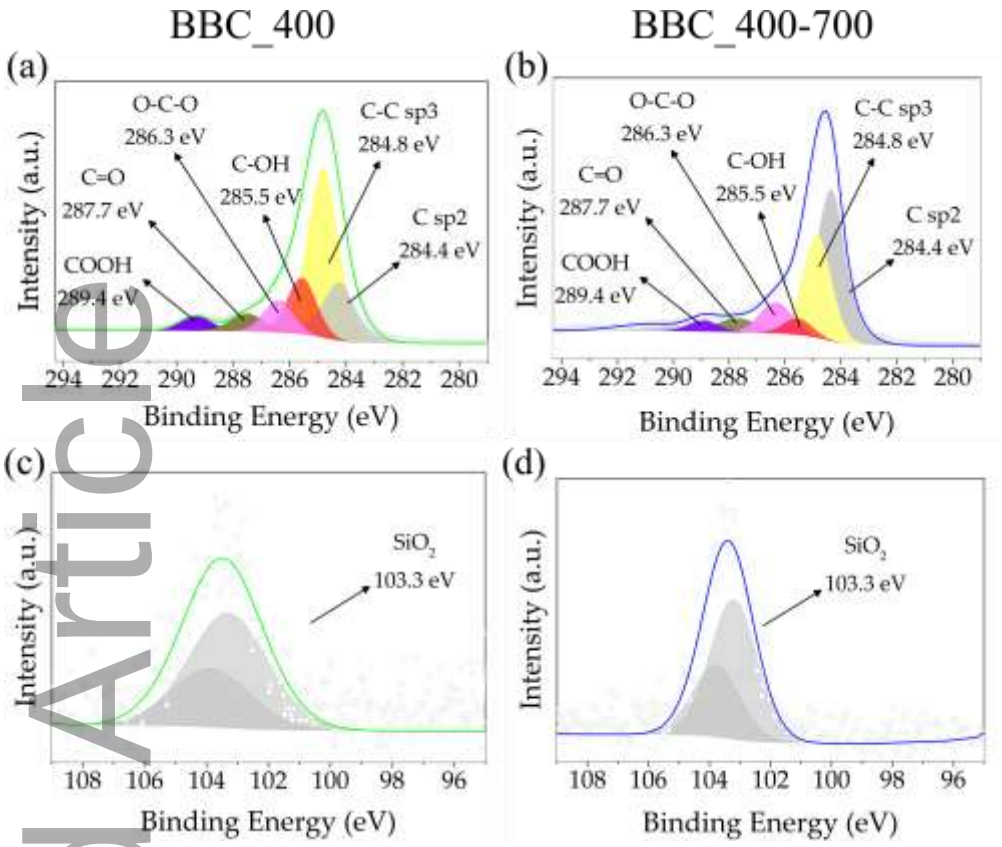

Figure 6. XPS spectra of BBCs materials: (a)-(b) C 1s spectrums of BBC_400 and BBC_400-700, respectively.(c)-(d) Si 2p spectrums of BBC_400 and BBC_400-700, respectively. Empty gray circles show the experimental data, and solid green/blue lines indicate the best fitting results after peak deconvolution.

The composition of C and Si in the BBC samples was determined by atomic absorption spectroscopy. These results found by this technique showed that the Si content (p/p) is 7.2 % and 7.8 % in BBC_400 and BBC_400-700 samples, respectively. As was previously discussed, the second pyrolysis step produces more decomposition of the raw material which explains the sligthly higher Si content on the second sample.

3.2. Electrochemical performance

The presence of a biocarbon decorated with SiO_x particles is very promising for its application in LIBs. Silicon has one of the highest theoretical specific capacity (3600 mAh g^{-1}) (ten times higher than graphite), but present the disadvantage of suffering around a 300 % volume change when lithiated. To addressed this drawback, in the last few years, numerous publications have proposed the use of carbon and silicon composites as a possible solution. These anodes work excellently since the carbon matrix increases the electrical conductivity

and provides mechanical resistance to tolerate the volume changes suffered by the silicates[35–37].

The electrochemical performance of the BBCs materials on lithium-ion half-cells were evaluated using metallic lithium as the counter and reference electrode. It is important to note that when using aqueous based CMC as a binder, the pH plays a critical role for Si-containing electrodes[38–40]. Taking this into consideration, the electrode slurries were prepared using either diluted phosphoric acid (pH 2) as solvent or water for comparison. The BBC_400_water and BBC_400_acid cycling performance are shown on **Figure S5**. For both BBC_400 cells initial capacities are around 2000 mAh g^{-1}, but quickly decay towards values close to 1000 mAh g^{-1} after ten cycles. This trend continues until reaching values of approximately 300 mAh g^{-1} after 100 cycles. For this material, no electrochemical changes were observed due to the slurry preparation conditions. **Figure 7a** shows cycling performance of BBC_400-700 cells. In this case, the electrochemical response is highly dependent on the pH values of the slurries. In the case of BBC_400-700_water the initial specific capacity is ~1200 mAh g^{-1} and then abruptly decays after 15 cycles. For BBC_400-700_acid a considerable improvement in capacity retention was observed, remaining the specific capacity ~2000 mAh g^{-1} for the first 20 cycles. **Figure 7b** shows the charge/discharge curves of the 5th cycle at 0.2C for BBC_400-700_water and BBC_400-700_acid electrodes. Both cells present the same profile with two marked plateaus corresponding to the lithiation-delithiation of SiO_2 [41,42] and to the insertion-deinsertion of Li^+ into the porous carbon structures. Discharge capacities of 1195 mAh g^{-1} and 1967 mAh g^{-1} were obtained for electrodes prepared in water and acid medium, respectively. Both capacities are far higher than the theoretical capacity of graphite i.e. 372 mAh g^{-1}, but the capacity of the electrode prepared using water as a binder is noticeably lower than the acidic one. These results confirm that the presence of SiO_2 particles - even in small percentages (7.8 %) - affect not only the specific capacity but also the conditions needed for the electrode preparation, affecting in the mechanical integrity of the electrode.

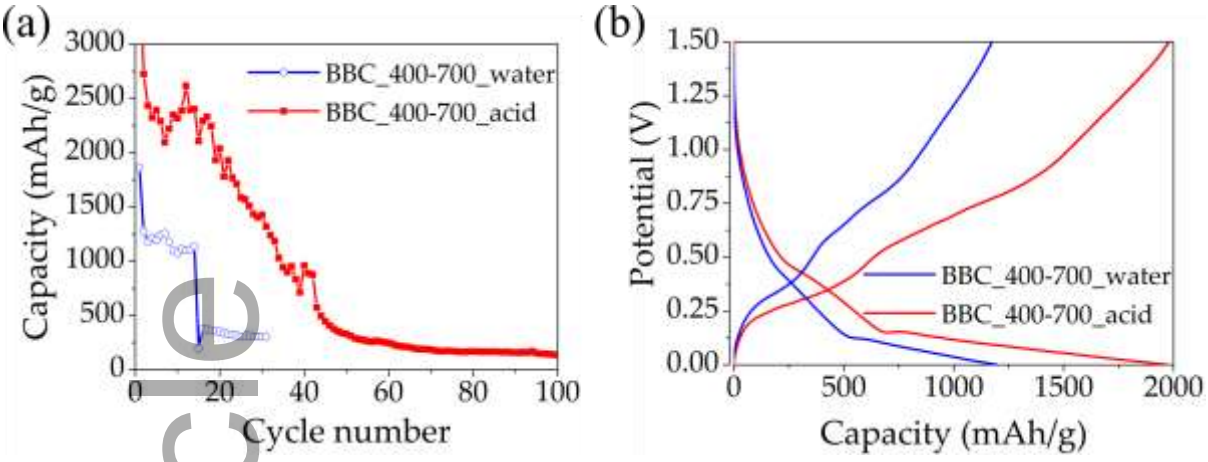

Figure 7. BBC_400-700_water and BBC_400-700_acid electrodes cycled at 0.2C: (a) Cycling performance, (b) Charge/discharge curves of the 5th cycle.

These results are in agreement with previous reports [38,43] which show that slurries prepared at a pH value lower than the Si particles' isoelectric point (IEP) (3.5) and pKa of CMC (3.5) present full neutralization of both the SiO- and COO- groups into SiOH and COOH groups. These features produce an increase in the mechanical strength of the composite electrode and its ability to reversibly sustain the volume variations of the silicon particles, which improves both capacity values and cyclability. As discussed before, BBC_400 material does not show noticeable changes for both slurry conditions. This could be due to the higher flexibility of the carbon matrix because of the lower degree of graphitization, as was previously discussed, and the fact that in this case the SiO_2 particles were covered as observed by SEM. The capacities obtained for BBC_400-700_acid during the first 20 cycles were shown to be up to 10 times higher than the ones for one pyrolysis step electrodes. Due to this noticeable improvement on capacity and cyclability obtained for the BBC_400-700_acid electrode, this sample was chosen for further electrochemical analysis.

Figure 8 presents the differential plot for a BBC_400-700_acid electrode. Two main signals can be clearly distinguished in the cathodic part of the plot. A broad peak around 0.43 V, corresponding to lithiation of SiO_2[44] and a second sharp peak at 0.15 V associated to the lithiation of Si (formed from SiO_2) [37,45] ; and/or to the Li^+ insertion into porous carbon structures[46,47].

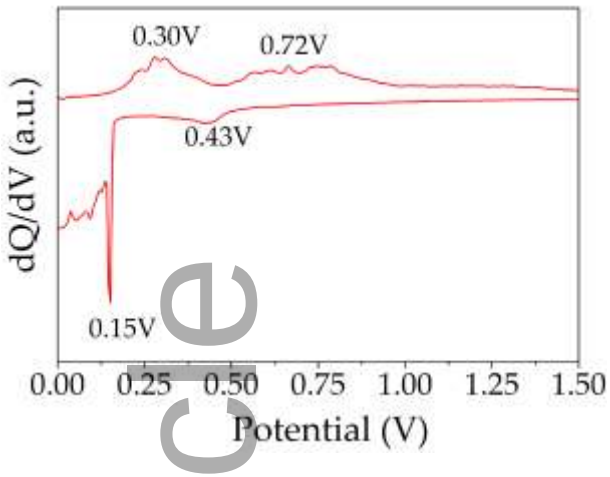

Figure 8. dQ/dV plot of the 5th cycle of BBC_400-700_acid electrode cycled at 0.2C.

These electrochemical results confirm that the use of BSG based biocarbon is responsible for the high specific capacity observed because it can i) act as a lithium reservoir, ii) favor the transportation paths, and iii) enhance the diffusion of Li^+ and penetration of electrolyte[48–51]. However, the interaction of inserted lithium with the oxygenated functional groups on the BBC material - detected by XPS measurements - could be another probable reason for the observed larger capacity together with the effect of the presence of SiO_2 particles.

In spite of the optimized slurry's preparation, the BBC_400-700_acid anode still decays quickly after 20 cycles (Figure 7a). This behavior could be related to inactivity on the lithium metal counter electrode due to the huge capacity of this anode. In order to solve this problem, a cell was cycled until the 30th cycle, disassembled and opened inside the Ar glovebox, in order to further reassembled it using a new fresh counter Li electrode. When the cell was disassembled, it was found that the BBC electrode was in good condition, no cracks or breaks were observed after cycling confirming the mechanical stability attained (**Figure S6**), so a new cell with the cycled electrode and fresh metallic lithium as the counter electrode was assembled and continued cycling at 0.2C (**Figure 9**) mantaining the specific capacity. After 130 cycles counter electrode was changed again for a fresh one, and an increase in the specific capacity from 447 mAh g^{-1} to 966 mAh g^{-1} was observed. The cell reassembled with fresh metallic lithium shows a noticeable improved capacity retention with respect to the cell presented in Figure 7. Therefore, the capacity decay observed during the first cycles corresponds to a depletion of metallic lithium instead of a problem with the working electrode, showing that BBC is a promising anode material for Li ion batteries.

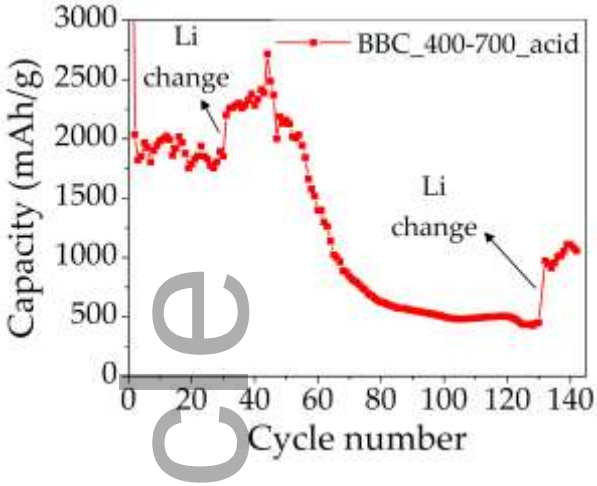

Figure 9. BBC_400-700_acid cycled until the 30th cycle, disassembled and reassemble with fresh metallic lithium cycled at 0.2C.

To further validate the performance of the BBC_400-700_acid anode for long term applications, its cyclability was tested at 0.5C. It is interesting to note (see **Figure S7**) that at higher current values, the specific capacities were lower than at 0.2C, but no refresh of the lithium counter electrode was necessary. Furthermore, a reversible capacity of 466 mAh g^{-1} was obtained, even after 100 cycles, outperforming the theoretical capacity of graphite.

For comparison, Table 1 shows several C/SiO_x biomass-derived carbons used as lithium-ion anode materials that are reported in the literature. Here we can observe that the biocarbon presented in this work not only shows the highest discharge capacity, but also present the most simple and sustainable synthesis procedure. The other works involve more complex, wasteful or unsustainable procedures, that use higher temperatures, require activation methods, and/or have many steps in order to obtain the final product[14,18,52,53]. In this sense, our proposed biocarbon is greener, generates less waste and is more ecofriendly.

Table 1. Comparative electrochemical performance of silicon/C biomass-based carbon material anodes for LIBs.

Biomass source	Synthesis method	Initial discharge capacity (mAh g-1)	C rate	Ref
Rice husk	Carbonized for 3 h at 500 °C. Activated with NaOH. 750 °C for 90 min	1908	0.2 C	[50]

Rice husk	Purification with HCl. Calcination 600 C 16 hs. Magnethotermic reduction	712	0.1 C	[51]
Rice husk	250 °C for 30 min. 2 h calcination at 700 °C. Treatment with HCl. Final carbonization at 700 °C	673	100 mA g^{-1}	[16]
Brewers' Spent Grains	Pyrolysis at 1000 °C for 3 h	514	0.1 C	[13]
Our work	Pre-calcination at 400 °C for 3h Second heating process at 700 °C for 2h	1967	0.2 C	This work

4. Conclusion

The development of high-performance and environmentally friendly energy storage devices is an urgent and important task for a sustainable future. In this context, the present study has successfully demonstrated the use of waste material from brewer spent grains to produce a promising anode material for Li-ion batteries. The simple and green synthesis process consisting of two low-temperature pyrolysis steps without any chemical treatment has yielded a biocarbon material with a high degree of graphitic phase, porosity, and exposed SiO_2 particles. These unique features have greatly enhanced the electrochemical behavior of the anode material, leading to outstanding capacity and cyclability performances. Notably, even though the amount of silicon oxide in the material is small, its presence has a direct influence on the electrode's electrochemical performance. Furthermore, the use of an aqueous binder in combination with the SiO_2 particles has significantly improved the mechanical stability of the electrode, which further contributes to its excellent cycling stability. Importantly, the developed anode material exhibits good stability and cyclability even after 100 cycles at 0.5C, with a specific capacity of 466 mAh g^{-1}, making it competitive with the state-of-the-art materials. Overall, this work provides a valuable contribution to the development of sustainable and efficient energy storage technologies, highlighting the potential of waste biomass-derived materials as viable alternatives for the production of high-performance Li-ion battery anodes.

Supporting Information

The following supporting Supporting Information is available from the Wiley Online Library. Figure S1: Differential thermal analysis of BSG, BBC_400, and BBC_400-700. Figure S2:

BBC_400 high magnification SEM micrography; Figure S3: BBCs EDS characterization; Figure S4: BBCs XPS survey spectra; Figure S5: BBC_400_water and BBC_400_acid cycling performance; Figure S6: BBC electrode and lithium after cycling pictures; Figure S7: BBC long cycling at 0.5 C.

Author Contributions

Conceptualization, Guillermina Luque and Sofía Raviolo; methodology, Guillermina Luque, Sofía Raviolo, Victoria Bracamonte, Fernando Cometto; formal analysis, Sofía Raviolo, Guillermina Luque, Victoria Bracamonte, Andrea Calderon, Fernando Cometto; investigation, Sofía Raviolo, Guillermina Luque, Victoria Bracamonte, Andrea Calderon, Fernando Cometto.; resources, Guillermina Luque, Andrea Calderón; data curation, Sofía Raviolo, Fernando Cometto; writing—original draft preparation, C.Andrea Calderón; Victoria Bracamonte; writing—review and editing, C.Andrea Calderón, Victoria Bracamonte, Fernando Cometto, Guillermina Luque; project administration, Guillermina Luque; funding acquisition, Guillermna Luque, Andrea Calderón. All authors have read and agreed to the published version of the manuscript.

Funding

This research was funded by Secyt-UNC, ANPCyT, PICT 2015-1605, PUE-22920170100092COINFIQC, and CONICET PIP 11220200102306CO, PICT 2018-3205.

Acknowledgments

The authors thank to Dr. Celso Quintero from Pontificia Universidad Católica de Chile for the elemental composition measurements; and Dr. Fernanda Stragliotto and Dr. Esteban Euti for the administrative support.

Conflicts of Interest

The authors declare no conflict of interest. The funders had no role in the design of the study; in the collection, analyses, or interpretation of data; in the writing of the manuscript; or in the decision to publish the results.

Data Availability Statement

The data that support the findings of this study are available from corresponding authors on request.

References

[1] M. F. Akorede, H. Hizam and E. Pouresmaeil, *Renewable and Sustainable Energy Reviews*, 2010, **14**, 724–734.
[2] J. M. Tarascon and M. Armand, *Nature*, 2001, **414**, 359–367.
[3] F. Luna-Lama, J. Morales and A. Caballero, *Materials*, 2021, **14**, 5995.
[4] B. Scrosati and J. Garche, *Journal of Power Sources*, 2010, **195**, 2419–2430.
[5] F. Huang, Q. Zhao, J. Yang, H. Zhang, W. Huo and F. Xu, *Energy Sources, Part A: Recovery, Utilization, and Environmental Effects*, 2018, **40**, 1675–1680.
[6] J. Du, J. Ma, Z. Liu, W. Wang, H. Jia, M. Zhang and Y. Nie, *RSC Adv.*, 2022, **12**, 20672–20678.
[7] Y.-N. Jo, M.-S. Park, E.-Y. Lee, J.-G. Kim, K.-J. Hong, S.-I. Lee, H. Y. Jeong, G. H. Ryu, Z. Lee and Y.-J. Kim, *Electrochimica Acta*, 2014, **146**, 630–637.
[8] M. del C. Rojas, M. L. Nieva Lobos, M. L. Para, M. E. González Quijón, O. Cámara, D. Barraco, E. L. Moyano and G. L. Luque, *Biomass and Bioenergy*, 2021, **146**, 105971.
[9] J. Alvarez, G. Lopez, M. Amutio, J. Bilbao and M. Olazar, *Bioresource Technology*, 2014, **170**, 132–137.
[10] J. Liu, B. Liu, C. Wang, Z. Huang, L. Hu, X. Ke, L. Liu, Z. Shi and Z. Guo, *Journal of Alloys and Compounds*, 2017, **718**, 373–378.
[11] M. Sieradzka, C. Kirczuk, I. Kalemba-Rec, A. Mlonka-Mędrala and A. Magdziarz, *Energies*, 2022, **15**, 1941.
[12] K. Jagiełło, W. Hińcz, W. Kaczorowska, M. Jackowski, M. Bartman and J. Kaczmarczyk, *Biomass Conv. Bioref.*, , DOI:10.1007/s13399-022-02964-6.
[13] S. Kane, A. Storer, W. Xu, C. Ryan and N. P. Stadie, *ACS Sustainable Chem. Eng.*, 2022, **10,** 12226–12233.
[14] S. D. Magar, C. Leibing, J. L. Gómez-Urbano, D. Carriazo and A. Balducci, *Energy Technology*, 2022, **10**, 2200379.
[15] A. F. C. Sousa, M. V. Gil and V. Calisto, *Environ Sci Pollut Res*, 2020, **27**, 36463–36475.
[16] E. Akhayere, E. A. Essien and D. Kavaz, *Environ Sci Pollut Res*, 2019, **26**, 25802–25813.
[17] H. Yang, R. Yan, H. Chen, D. H. Lee and C. Zheng, *Fuel*, 2007, **86**, 1781–1788.
[18] Y. Guo, X. Chen, W. Liu, X. Wang, Y. Feng, Y. Li, L. Ma, B. Di and Y. Tian, *J. Electron. Mater.*, 2020, **49**, 1081–1089.
[19] T. Rao Penki, Kishore, B. N. Munichandraiah and D. Shanmughasundaram, *Advanced Materials Letters*, 2014, **5**, 184–190.
[20] W. Suliman, J. B. Harsh, N. I. Abu-Lail, A.-M. Fortuna, I. Dallmeyer and M. Garcia-Perez, *Biomass and Bioenergy*, 2016, **84**, 37–48.
[21] M. Uchimiya, L. H. Wartelle, K. T. Klasson, C. A. Fortier and I. M. Lima, *J. Agric. Food Chem.*, 2011, **59**, 2501–2510.

[22] M. V. Bracamonte, G. I. Lacconi, S. E. Urreta and L. E. F. Foa Torres, *J. Phys. Chem. C*, 2014, **118**, 15455–15459.
[23] M. A. Pimenta, G. Dresselhaus, M. S. Dresselhaus, L. G. Cançado, A. Jorio and R. Saito, *Phys. Chem. Chem. Phys.*, 2007, **9**, 1276–1290.
[24] R. Azargohar, S. Nanda, J. A. Kozinski, A. K. Dalai and R. Sutarto, *Fuel*, 2014, **125**, 90–100.
[25] Y. Shao, C. Guizani, P. Grosseau, D. Chaussy and D. Beneventi, *Carbon*, 2018, **129**, 357–366.
[26] N. Tripathi, A. R. Uribe, H. Weldekidan, M. Misra and A. K. Mohanty, *Mater. Adv.*, 2022, **3**, 9071–9082.
[27] M. Giorcelli, P. Savi, A. Khan and A. Tagliaferro, *Biomass and Bioenergy*, 2019, **122**, 466–471.
[28] Z. Li, B. Delvaux, J. Yans, N. Dufour, D. Houben and J.-T. Cornelis, *Journal of Plant Nutrition and Soil Science*, 2018, **181**, 537–546.
[29] S. Kaciulis, *Surf. Interface Anal.*, 2012, **44**, 1155–1161.
[30] X. Chen, X. Wang and D. Fang, *Fullerenes, Nanotubes and Carbon Nanostructures*, 2020, **28**, 1048–1058.
[31] R. Al-Gaashani, A. Najjar, Y. Zakaria, S. Mansour and M. A. Atieh, *Ceramics International*, 2019, **45**, 14439–14448.
[32] X.-Q. Lin, Q.-F. Lü, Q. Li, M. Wu and R. Liu, *ACS Omega*, 2018, **3**, 13283–13289.
[33] X. Xin, X. Zhou, F. Wang, X. Yao, X. Xu, Y. Zhu and Z. Liu, *J. Mater. Chem.*, 2012, **22**, 7724–7730.
[34] H. Kim, M. Seo, M.-H. Park and J. Cho, *Angewandte Chemie International Edition*, 2010, **49**, 2146–2149.
[35] F. Jeschull, F. Lindgren, M. J. Lacey, F. Björefors, K. Edström and D. Brandell, *Journal of Power Sources*, 2016, **325**, 513–524.
[36] X. Zhao and V.-P. Lehto, *Nanotechnology*, 2021, **32**, 042002.
[37] G. Lener, A. A. Garcia-Blanco, O. Furlong, M. Nazzarro, K. Sapag, D. E. Barraco and E. P. M. Leiva, *Electrochimica Acta*, 2018, **279**, 289–300.
[38] A. Tranchot, H. Idrissi, P. X. Thivel and L. Roué, *J. Electrochem. Soc.*, 2016, **163**, A1020–A1026.
[39] U. S. Vogl, P. K. Das, A. Z. Weber, M. Winter, R. Kostecki and S. F. Lux, *Langmuir*, 2014, **30**, 10299–10307.
[40] E. N. Primo, F. Eroles, M. del C. Rojas, F. Cometto, E. Leiva, D. E. Barraco and G. L. Luque, *Journal of Power Sources*, 2023, **563**, 232800.
[41] C. C. Nguyen, T. Yoon, D. M. Seo, P. Guduru and B. L. Lucht, *ACS Appl. Mater. Interfaces*, 2016, **8**, 12211–12220.
[42] W.-F. Ren, Y. Zhou, J.-T. Li, L. Huang and S.-G. Sun, *Current Opinion in Electrochemistry*, 2019, **18**, 46–54.
[43] C. E. L. Foss, S. Müssig, A. M. Svensson, P. J. S. Vie, A. Ulvestad, J. P. Mæhlen and A. Y. Koposov, *Sci Rep*, 2020, **10**, 13193.
[44] M. Li, Y. Zeng, Y. Ren, C. Zeng, J. Gu, X. Feng and H. He, *Journal of Power Sources*, 2015, **288**, 53–61.
[45] Y. Feng, X. Liu, L. Liu, Z. Zhang, Y. Teng, D. Yu, J. Sui and X. Wang, *ChemistrySelect*, 2018, **3**, 10338–10344.
[46] R. Guo, L. Zhao and W. Yue, *Electrochimica Acta*, 2015, **152**, 338–344.
[47] D. Saikia, T.-H. Wang, C.-J. Chou, J. Fang, L.-D. Tsai and H.-M. Kao, *RSC Adv.*, 2015, **5**, 42922–42930.
[48] T. Kasuh, A. Mabuchi, K. Tokumitsu and H. Fujimoto, *Journal of Power Sources*, 1997, **68**, 99–101.

[49] Y.-P. Wu, C.-R. Wan, C.-Y. Jiang, S.-B. Fang and Y.-Y. Jiang, *Carbon*, 1999, **12**, 1901–1908.
[50] J. R. Dahn, T. Zheng, Y. Liu and J. S. Xue, *Science*, 1995, **270**, 590–593.
[51] K. Sato, M. Noguchi, A. Demachi, N. Oki and M. Endo, *Science*, 1994, **264**, 556–558.
[52] K. Yu, J. Li, H. Qi and C. Liang, *Diamond and Related Materials*, 2018, **86**, 139–145.
[53] N. Kalidas, J. Riikonen, W. Xu, K. Lahtinen, T. Kallio and V. P. Lehto, *Materials Chemistry and Physics*, 2020, **245**, 122736.

Table of Contents

Sofía Raviolo*, M. Victoria Bracamonte, Cecilia A. Calderón, Fernando P. Cometto and Guillermina L. Luque*

Synthesis and characterization of outstanding anodic material for lithium-ion batteries was produced using a carbon/silica compound derived from waste material generated by the brewing industry (BSG) through a low-polluting method. The obtained biocarbon possesses specific capacity value that is almost five times greater than the conventional graphite anode material used in commercial lithium-ion batteries